Identifying lipid traces of atherogenic mechanisms in human carotid plaque

Slijkhuis, N.; Towers, M.; Mirzaian, M.; Korteland, S.A.; Heijs, B.; Gaalen, K. van; ... ; Soest, G. van

Atherosclerosis 385 (2023) 117340

Contents lists available at ScienceDirect

Atherosclerosis

journal homepage: www.elsevier.com/locate/atherosclerosis

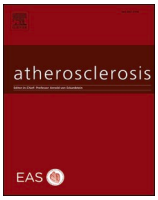

Identifying lipid traces of atherogenic mechanisms in human carotid plaque

Nuria Slijkhuis [a], Mark Towers [b], Mina Mirzaian [c], Suze-Anne Korteland [a], Bram Heijs [d], Kim van Gaalen [a], Ingeborg Nieuwenhuizen [a], Alex Nigg [e], Kim van der Heiden [a], Yolanda B. de Rijke [c], Aad van der Lugt [f], Eric J.G. Sijbrands [g], Emmanuelle Claude [b], Gijs van Soest [a,h,*]

[a] Department of Cardiology, Erasmus MC, University Medical Center Rotterdam, the Netherlands
[b] Waters Corporation, Wilmslow, United Kingdom
[c] Department of Clinical Chemistry, Erasmus MC, University Medical Center Rotterdam, the Netherlands
[d] Center for Proteomics and Metabolomics, Leiden University Medical Center, Leiden, the Netherlands
[e] Optical Imaging Center, Erasmus MC, University Medical Center Rotterdam, the Netherlands
[f] Department of Radiology and Nuclear Medicine, Erasmus MC, University Medical Center Rotterdam, the Netherlands
[g] Department of Internal Medicine, Erasmus MC, University Medical Center Rotterdam, the Netherlands
[h] Department of Precision and Microsystems Engineering, Faculty of Mechanical Engineering, Delft University of Technology, Delft, the Netherlands

ARTICLE INFO

Keywords:
Atherosclerosis
Desorption electrospray ionization-mass spectrometry imaging
Lipidomics
Plaque destabilization
Histology
Carotid endarterectomy

ABSTRACT

Background and aims: Lipids play an important role in atherosclerotic plaque development and are interesting candidate predictive biomarkers. However, the link between circulating lipids, accumulating lipids in the vessel wall, and plaque destabilization processes in humans remains largely unknown. This study aims to provide new insights into the role of lipids in atherosclerosis using lipidomics and mass spectrometry imaging to investigate lipid signatures in advanced human carotid plaque and plasma samples.
Methods: We used lipidomics and desorption electrospray ionization mass spectrometry imaging (DESI-MSI) to investigate lipid signatures of advanced human carotid plaque and plasma obtained from patients who underwent carotid endarterectomy ($n = 14$ out of 17 whose plaque samples were analyzed by DESI-MSI). Multivariate data analysis and unsupervised clustering were applied to identify lipids that were the most discriminative species between different patterns in plaque and plasma. These patterns were interpreted by quantitative comparison with conventional histology.
Results: Lipidomics detected more than 300 lipid species in plasma and plaque, with markedly different relative abundances. DESI-MSI visualized the spatial distribution of 611 lipid-related *m/z* features in plaques, of which 330 *m/z* features could be assigned based on exact mass, comparison to the lipidomic data, and high mass resolution MSI. Matching spatial lipid patterns to histological areas of interest revealed several molecular species that were colocalized with pertinent disease processes in plaque including specific sphingomyelin and ceramide species with calcification, phospholipids and free fatty acids with inflammation, and triacylglycerols and phosphatidylinositols with fibrin-rich areas.
Conclusions: By comparing lipid species in plaque and plasma, we identified those circulating species that were also prominently present in plaque. Quantitative comparison of lipid spectral patterns with histology revealed the presence of specific lipid species in destabilized plaque areas, corroborating previous *in vitro* and animal studies.

1. Introduction

Ischemic stroke remains a leading cause of death and severe disability worldwide [1]. Atherosclerosis of the carotid artery is a common underlying pathology of ischemic stroke. The accumulation of lipids and inflammatory cells in the arterial wall results in the formation of plaque [2]. When a plaque ruptures, its content comes in contact with the bloodstream triggering thrombus formation, which subsequently blocks the blood flow causing ischemic stroke. The risk of rupture depends on plaque composition, critically impacting biomechanical stability. Plaques most prone to rupture are characterized by a large lipid-rich necrotic core covered by a thin fibrous cap, many

* Corresponding author. P.O. Box 2040, 3000 CA, Rotterdam, the Netherlands.
E-mail address: g.vansoest@erasmusmc.nl (G. van Soest).

https://doi.org/10.1016/j.atherosclerosis.2023.117340
Received 27 April 2023; Received in revised form 5 October 2023; Accepted 10 October 2023
Available online 11 October 2023

inflammatory cells, and intra-plaque hemorrhage [3]. However, the significant local variation in plaque phenotype makes accurately predicting the evolution of plaques and clinical outcomes challenging, ultimately leading to suboptimal risk stratification [4].

Lipidomic plasma analyses have yielded several circulating lipid species that are associated with an increased risk of cardiovascular events [5,6]. However, the relationship between circulating lipids and plaque pathobiology remains poorly understood, and mechanisms linking the two are largely unknown. Lipids are both by-products of disease processes and active mediators of, for instance, inflammation [7,8]. *In vitro* and animal studies have identified mechanistic links between specific lipids, such as sphingomyelins [9,10], ceramides [11] and cholesteryl esters [12], and atherogenic processes, but these have not been studied in humans. We hypothesized that spatial lipidomics of human atherosclerotic plaque can support these associations by revealing the colocalization of these lipids with atherosclerotic disease processes.

Desorption electrospray ionization mass spectrometry imaging (DESI-MSI) is a molecular imaging technique that can detect and visualize a wide range of lipid species in tissue sections in a label-free manner [13]. Molecules in the tissue sections are first ionized using a fine nebulized spray of charged micro-droplets aimed at the tissue section. Subsequently, the ions travel into a mass analyzer, which, for the purposes of our study, was set to a specific mass range of 100 to 1200 Da. In the mass analyzer, the mass-to-charge ratios (m/z) of the ions are measured and converted to a mass spectrum displaying all m/z values. During DESI-MSI acquisition, tissue sections are raster scanned, and mass spectra recorded with X and Y coordinates are generated, which preserves the spatial distribution of each detected molecule. The pixel size in DESI-MSI, which reflects the spatial resolution, depends on the specific setup and configuration. Recent advancements in the technology have led to increased resolution capabilities down to 20 μm. Hence, DESI-MSI gives detailed information about the spatial lipid distribution on a molecular level.

This study aims to provide new insights into the role of lipids in atherosclerosis using lipidomics and dual-polarity high spatial resolution DESI-MSI to investigate lipid signatures in advanced human carotid plaque and plasma samples from the same patients who underwent carotid endarterectomy. Previous studies have also utilized MSI to investigate lipids in atherosclerotic plaque. For example, secondary ion mass spectrometry (SIMS) was used to analyze the lipid distribution in human coronary arteries in the context of lesion characteristics and severity [14]. Additionally, matrix-assisted laser desorption-ionization (MALDI) MSI and DESI-MSI have been used for the detection of lipids in atherosclerotic plaques from mice [15,16] and human [17–20]. However, past DESI-MSI studies were limited in their capacity to detect a broad range of lipid species, most likely due to sensitivity constraints. Furthermore, MALDI and SIMS often encounter in-source fragmentation and their sample preparation methods can influence the lipids detected. The differences between mice and humans also call for cautious interpretation when translating findings. With these limitations in mind, the present study employs DESI-MSI with minimal in-source fragmentation, simple sample preparation, and enhanced detection efficiency. By using DESI-MSI in positive and negative ionization mode, we were able to detect 25 different lipid classes. This represents a significant advancement, making this study the first to map the spatial distribution of all major known lipid classes relevant to atherosclerosis at high image resolution. The quantitative comparison of lipid spectral patterns with histology identified prominent plaque lipids, relative to plasma, located in human carotid plaque areas colocalized with destabilization, corroborating previous *in vitro* and animal studies. These findings provide clues to lipidomic signatures of disease mechanisms that drive atherosclerotic plaque evolution.

2. Materials and methods

An overview of the methodology of this study is shown schematically in Fig. 1 and is described in detail in the sections below.

2.1. Sample collection

Seventeen carotid plaques were obtained from symptomatic patients who underwent carotid endarterectomy. Corresponding plasma samples were obtained from these patients in a non-fasted state one day prior to surgery and subsequently stored at −80 °C. Plaques were snap-frozen in liquid nitrogen and stored at −80 °C until further processing. Upon further processing, plaques were cut in 3 mm cross-sections. One 3 mm cross-section from each plaque was used for plaque lipidomics. Out of 17 plaques, 14 were sufficiently intact for DESI-MSI. The cross-section with the highest plaque burden was selected for DESI-MSI. Written informed consent was obtained from all patients and ethical guidelines were approved by the Erasmus Medical Center Ethics Board and followed during sample collection and processing (MEC 2018–079).

2.2. Plaque and plasma lipidomics

The Lipidyzer platform was used to detect lipid species in both plaque homogenates and plasma samples. The platform consists of a SCIEX QTRAP 5500 mass spectrometer (AB Sciex, Framingham, United States) with a SelexION differential ion mobility interface and a Nexera X2 SIL-30AC ultrahigh-performance liquid chromatography (Shimadzu, Kyoto, Japan) operated with Analyst software. Plaque homogenates were prepared by grinding one snap-frozen 3 mm cross-section of every plaque into a fine powder, diluting the weight of the powder ten times using methanol:water 15:85 (%v/v) solution and homogenizing the suspension using a TissueLyser LT (QIAGEN) with glass beads. Lipid extraction for plaque homogenates and plasma was performed using a modified Bligh-Dyer extraction protocol according to the Lipidyzer protocol. In short, 50 μL of plaque homogenate or plasma was used for liquid-liquid extraction using water, methanol, and dichloromethane (DCM). Then, 50 μL of internal standard mix solution (AB Sciex, Framingham, United States), containing 54 isotopically labeled internal standards across 13 lipid classes, was added to the samples. The lower phase (DCM) containing the lipids was transferred to a clean tube. Then the procedure was repeated by performing another extraction by adding DCM to the upper phase and interphase. The DCM phases were pooled and dried under a stream of nitrogen. The residue was dissolved in Lipidyzer eluent containing 10 mM ammonium acetate in methanol:DCM 1:1 (v/v) and was delivered to the autosampler. For data analysis, we used the lipid species composition data of the Lipidyzer platform. This is the relative contribution of each lipid species (e.g., phosphatidylcholine (36:2)) within its lipid class (e.g., phosphatidylcholines) calculated as a percentage, which was normalized to 100 % per lipid class.

2.3. Multivariate analysis of lipidomics data

Multivariate analysis was employed to compare plaque and plasma lipid content to identify the circulating species that accumulate prominently in plaque. An orthogonal projections to latent structures discriminant analysis (OPLS-DA) model was fitted in SIMCA 17 (Umetrics, Sweden) for all plasma and plaque lipids. In the model, the lipid composition percentages per class were defined as variables and sample IDs as observations. The quality of fit was reported as R^2, and the predictability of the model was reported as Q^2. The model was considered significant when $R^2 > 0.5$ and $Q^2 > 0.5$ and was further validated with a permutation test and by sevenfold cross-validation analysis of variance (CV-ANOVA). Variable influence on projection (VIP) values above 1.0 were considered significant in influencing the separation of plasma and plaque samples.

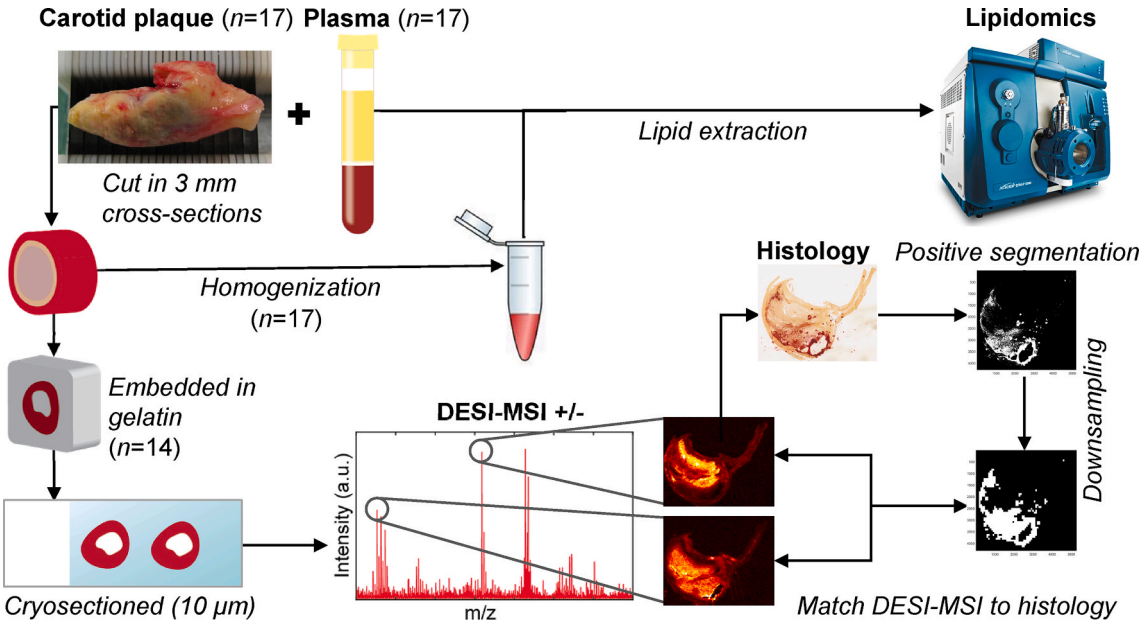

Fig. 1. Schematic overview of the study design.

2.4. MSI and histology sample preparation

To conduct DESI-MSI measurements, the 3 mm cross-section with the highest plaque burden from each plaque ($n = 14$) was embedded in 10 % porcine type A gelatin (Sigma-Aldrich, The Netherlands), snap-frozen, and stored at −80 °C until cryosectioning. Cryosectioning (CM3050 S, Leica Biosystems) was performed at −20 °C with a cutting thickness of 10 µm. Sections were thaw-mounted onto glass slides and stored at −80 °C until further usage. Per plaque, two glass slides were used for DESI-MSI measurements in positive and negative ionization mode, and eight glass slides were used for histology. Additionally, one plaque was selected for MALDI-FTICR-MSI measurements, one slide was used for positive ionization mode and one slide was used for negative ionization mode. For these measurements an organic matrix (2,5-dihydroxybenzoic acid for positive ionization mode, and 1,5-diaminonaphthalene for negative ionization mode) was sublimated onto the tissue sections.

2.5. DESI-MSI measurements

DESI-MSI measurements were performed on a Synapt XS mass spectrometer with a DESI-XS source (Waters, Wilmslow, United Kingdom) in positive and negative ionization mode. All measurements were performed in sensitivity mode. DESI spray solvent was methanol: water 98:2 (%*v*/*v*) (Honeywell, Germany), which was delivered with a solvent flow rate of 2 µL/min. The capillary voltage was optimized between 0.6 and 0.8 kV, and the nitrogen gas pressure was 69–103 kPa (10–15 psi). A heated transfer line was used at 370 °C to improve ionization and transmission of the molecules into the mass spectrometer. All samples were measured with a pixel size of 100 × 100 µm^2. Additionally, a subset of samples ($n = 4$) was measured with a pixel size of 20 × 20 µm^2 in positive ionization mode. The mass range was *m/z* 100–1200, and the scan acquisition rate was two scans per second. Data were acquired using MassLynx v4.2 software. Lock mass correction was performed on the raw data using a prominent and known lipid species, namely SM(34:1) $[M+Na]^+$ (*m/z* 725.5) in positive ion mode and Cer (34:1) $[M+Cl]^-$ (*m/z* 572.5) in negative ion mode. HDI v1.4 software was used to export the data in imzML format (Waters, Wilmslow, United Kingdom). An in-house developed data processing pipeline [21] in MATLAB™ 2017a (The Mathworks, Inc., Natick, Massachusetts, USA) was used in combination with mMass software [22] to select lipid *m/z* features and remove isotopes. For further data analysis, a subset of lipid *m/z* features was selected that were present in at least five out of fourteen samples.

2.6. Lipid annotation

Identity assignment of lipid-related *m/z* features in the DESI-MSI data was performed using two complementary approaches. We first created a list of lipid species detected with the Lipidyzer platform in the plaque homogenates. The exact *m/z* with possible adducts of the lipid identities were obtained from the Lipid Maps database [23] and matched to the DESI-MSI *m/z* values.

Additionally, we performed high-mass-resolution measurements using MALDI-FTICR-MSI on the most lipid-rich plaque section. MALDI-FTICR-MSI measurements were conducted using a Bruker Daltonics solariX xR mass spectrometer equipped with a 12 T superconductive magnet, a dynamically harmonized ParaCell™, and a Combi-Source™. The system was controlled using ftmsControl (v2.10 Build 98, Bruker Daltonics). The data were collected with a transient length of 3.3554 s (4 M data points in the time domain), resulting in an estimated resolution of 776,000 at *m/z* 400. The MALDI source was equipped with a SmartBeam™-II laser ($\lambda = 355$ nm) operating at 200 Hz and 15 % power and using the "Small" focusing setting (ablation area approximately 70 × 70 µm^2). The measurements were performed in positive and negative ionization mode with a pixel size of 100 × 100 µm^2. The MALDI matrices used were 2,5-dihydroxybenzoic acid (Sigma Aldrich, The Netherlands) for positive ionization mode (sublimation, 50 mg dissolved in 5 ml aceton, 125 °C, 10 min), and 1,5-diaminonaphthalene (Sigma Aldrich, The Netherlands) for negative ionization mode (sublimation, 50 mg dissolved in 5 ml acetonitrile, 145 °C, 20 min). A total of 50 shots per pixel were acquired, covering a mass range between *m/z* 300–1200. Data were converted to imzML format using SCiLS Lab software (v2016b, Bruker Daltonics) for further processing. FTICR data was processed with an in-house developed data processing pipeline [21] in MATLAB™ 2017a (The Mathworks, Inc., Natick, Massachusetts, USA) in combination with mMass software [22] for peak picking and isotope removal. Lipid *m/z* values were matched to the exact *m/z* values with possible adducts of the identities found with the Lipidyzer platform to increase confidence in identifications. Lipid annotations were considered when the mass error was under 15 parts per million (ppm).

2.7. Histology

Tissue sections consecutive to the section used for DESI-MSI analysis were stained by hematoxylin & eosin (HE) (VWR, The Netherlands), Oil Red O (ORO) (Sigma Aldrich, The Netherlands), Martius Scarlet Blue (MSB) (Martius Yellow, Brilliant Crystal Scarlet, Aniline Blue) (Sigma Aldrich, The Netherlands), Alizarin Red S (Sigma Aldrich, The Netherlands), Miller's elastin stain (VWR, The Netherlands), and the immunohistochemical stains Recombinant Anti-CD68 antibody (Abcam, United Kingdom), polyclonal rabbit a-human acid sphingomyelinase (ASMase) (BS-6318R, Bio-connect, The Netherlands), and Mouse anti-human Anti- Apolipoprotein B100 (ApoB) (LS-B13962–0.5, Bio-connect, The Netherlands). Whole slides were digitized with a Nanozoomer 2.0HT slide scanner (Hamamatsu Photonics, Hamamatsu, Japan) at 20× magnification with a pixel size of 0,455 μm. Quantification of calcified plaque areas (Alizarin-Red S), macrophage-infiltrated areas (CD68 antibody), fibrin-rich areas (MSB), lipid-rich areas (ORO), ASMase positive areas, and ApoB positive areas were performed using Visiopharm software (Horsholm, Denmark, version 2022.07). The slide images were imported in the Visiopharm image analysis software, and rough tissue detection was done by a deep learning algorithm (U-Net) at 2× input magnification to reduce the area to be measured at higher magnification. Artifacts were manually excluded from the analysis. Per staining, an algorithm was designed on normalized images at 20× input magnification by setting a threshold for the stained features of interest. Precise positive and total tissue areas were measured per section, and the percentage of positively stained areas was calculated by (positive area/total area)*100.

2.8. Quantification of the colocalization of positive histological areas and DESI images

A MATLAB™ 2019b pipeline was developed to match positive histological regions of interest as defined by Visiopharm software (calcifications, macrophages, and fibrin) with DESI-MSI images to quantify the colocalization of lipid spectral patterns with these areas. The Visiopharm TIF image of histology containing the positive histological segmentation was registered to the total ion current (TIC) image of the DESI-MSI sample. The positive stained region image was down-sampled by block-averaging to match the resolution of the DESI-MSI images. Then, the transform of the registration was applied to the down-sampled positive mask, which was matched with the 10 % most intense pixels of every DESI-MSI lipid image. Some plaque samples were excluded from the analysis. For calcified regions, 4 plaque samples were excluded from the colocalization efforts due to heavy calcification. This made the lipid distributions nonspecific to these calcified areas, leaving us with 10 samples for this particular analysis. For CD68 positive and fibrin-rich regions, samples with a positive histological area of ≤1 % were excluded (n = 1 and n = 5, respectively) since these areas were too small and scattered to match with DESI-MSI images. This resulted in the analysis of 13 samples for colocalization analysis with CD68 positive regions, and 9 samples for the colocalization analysis with fibrin-rich regions. A list was generated showing the percentage of the most intense pixels that colocalize with histological regions for each DESI-MSI image.

2.9. Unsupervised clustering algorithm

A non-negative matrix factorization (NMF) algorithm was applied to the combined DESI-MSI spectral data of all tissue sections to reduce dimensionality. An NMF toolbox for biological data mining was used [24,25]. The optimal number of clusters was calculated based on dispersion coefficients.

3. Results

3.1. Sample characteristics

We collected 17 plasma and 17 carotid plaque samples from patients who underwent carotid endarterectomy. Our patient population consisted of 10 male and 7 female patients with a mean age of 69 years with a standard deviation of 9 years. Detailed patient characteristics can be found in Supplementary Table S1. Fourteen plaque samples were sufficiently intact to employ DESI-MSI and histology.

3.2. Plasma and plaque lipid class composition

We detected 330 and 310 lipid species from 13 different lipid classes in plasma and plaque homogenates, respectively, using the Lipidyzer platform. We compared the lipid class composition of plasma and plaque samples; Fig. 2A displays the relative distribution (expressed as average 10-log percentage composition) of each lipid class in plasma and plaque. Plasma lipids consisted on average of 37% cholesteryl esters (CEs), 22% triacylglycerol (TAG), 21 % phosphatidylcholine (PC), 8% free fatty acid (FFA), 6% sphingomyelin (SM), 3% lysophosphatidylcholine (LPC), 2% phosphatidylethanolamines (PE), 1% diacylglycerol (DAG), 0.2% ceramide (Cer), which include dihydroceramide (DCer), hexosylceramide (HexCer) and lactosylceramide (LacCer), and 0.1% lysophosphatidylethanolamines (LPE). Plaque homogenates consisted on average of 63% CE, 10% SM, 7% TAG, 7% FFA, 5% PC, 3% DAG, 3% LPC, 2% PE, 1% Cer (including DCer, HexCer, and LacCer) and 0.4% LPE.

3.3. Comparison of lipid spectra in plasma and plaque

Differences between the lipid class composition of plasma and plaque can be refined by unraveling the differences on the species level. An OPLS-DA multivariate model, see Supplementary Fig. S2, resulted in significant parameters, namely, R^2 of 0.99 and a Q^2 of 0.97, and a p-value of 3.80E-23 as calculated by CV-ANOVA. Fig. 2B displays the loadings of the OPLS-DA model, with the lipids near the blue and orange star being more prevalent in plaque and plasma, respectively. The size of the circles represents the relative abundance of the lipid species in plaque. The lipids with the strongest influence (VIP >1.0) on the separation between plasma and plaque and their relative abundance in plaque compared to plasma are listed in Supplementary Table S2 and S3. The lipids contributing to the separation of plasma and plaque samples that were elevated in plaque were 18 FFAs, 2 PCs, 2 Cers, 4 PEs, 3 SMs, 28 TAGs, 3 LacCer, 1 DAG, 14 CEs, 1 DCer, 7 LPCs, and 2 HexCer.

The FFA lipid class had the largest influence (high VIP) on the separation between plaque and plasma, with 18 out of 20 species with a VIP >1.0 being more prevalent in plaque compared to plasma. The three FFAs with the highest VIP values were FFA(12:0), FFA(20:3), and FFA (20:2). While FFA(18:1) and FFA(16:0) were the most abundant species within the FFA class in both plasma and plaque, the ratio FFA(18:1)/FFA (16:0) differed between plasma and plaque, namely 1.28 and 0.61, respectively. We found two PC species relatively enriched in plaque, PC (32:0) and PC(34:1), and 16 PC species with a VIP >1.0 that were more abundant in plasma. The relatively elevated SM species in plaque were SM(34:1), SM(42:1), and SM(32:1). Interestingly, SM(34:1) constituted almost half (45 %) of all SM species in plaque, while it comprised 26 % of the SM species in plasma, see Fig. 3A. When looking at Cer, we found 8 species with a VIP >1.0. Two of those were more present in plaque compared to plasma, namely Cer(34:1) and Cer(36:1). Similar to SM (34:1), Cer(34:1) constituted a large part, that is 40 % of the total Cer content, in plaque. In contrast, Cer(34:1) made up less than 10 % of the Cer content in plasma, see Fig. 3A. Another prominent lipid differentiating plasma from plaque lipids is DAG(40:0). DAG(40:0) constituted 65 % of the total DAG content of plaque, while for plasma DAG(40:0) comprised less than 1 % of the total DAG content. Lastly, of the 15 CE species with a VIP >1.0, only CE(18:2) was lower in plaque compared to

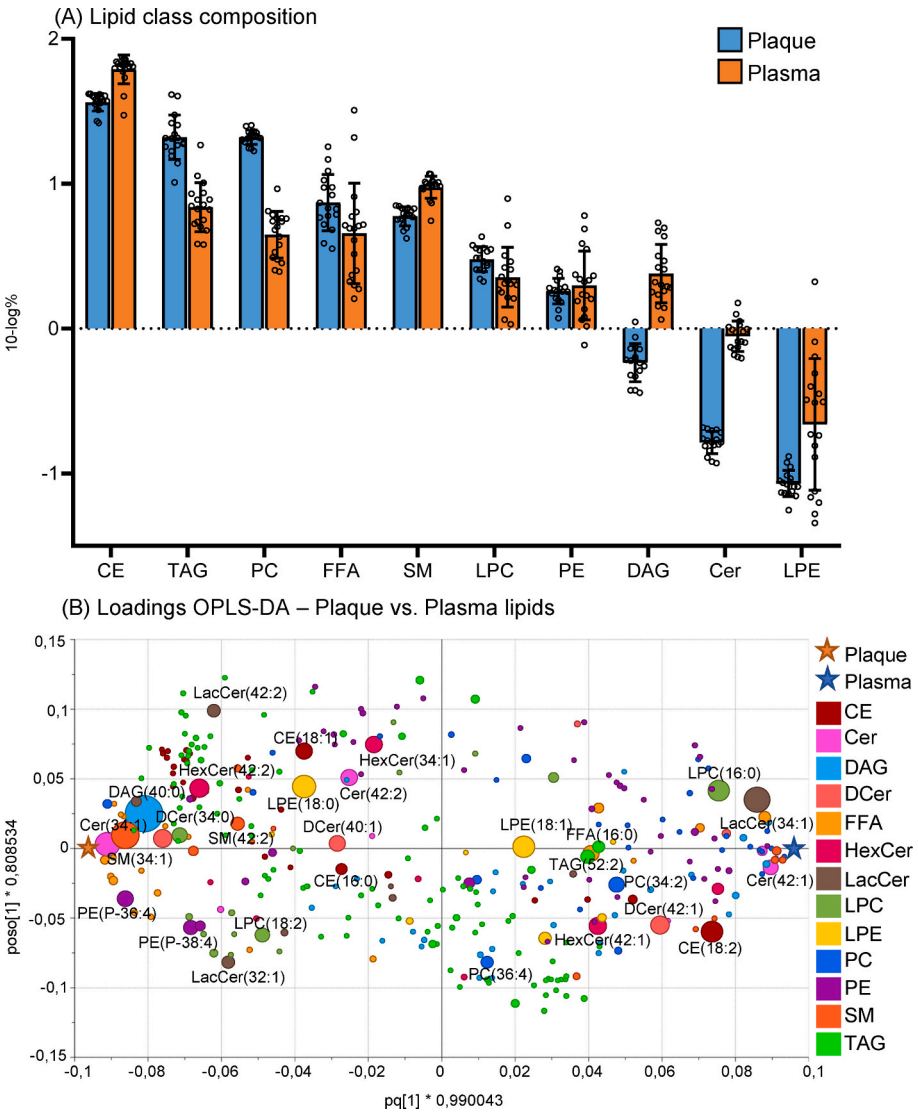

Fig. 2. Comparison of lipid classes and individual species between plasma and plaque samples.
(A) Average lipid class composition of plasma and plaque samples in 10-log percentages with error bars representing the standard deviation, and circles representing all individual data points. (B) Loadings of the OPLS-DA model discriminating plaque and plasma samples based on their lipid content. Lipid species near the orange star are relatively more present in plaque samples, while lipids near the blue star are relatively more present in plasma. The size of the circles indicates the average overall abundance in plaque: for example, LPC(16:0), LacCer(34:1), Cer(42:1), and CE(18:2) are more prominent in plasma, but also relatively abundant in plaque samples. (For interpretation of the references to colour in this figure legend, the reader is referred to the Web version of this article.)

plasma. CE(18:2) and CE(18:1), also known as cholesteryl linoleate and cholesteryl oleate, make up the majority of the total CE content in both plasma (65 %) and plaque (56 %). However, their CE(18:2)/CE(18:1) ratio differs, namely 2.08 for plasma and 1.42 for plaque.

3.4. *DESI-MSI visualized 611 lipid species from 25 different lipid classes*

DESI-MSI analysis identified 611 lipid-related *m/z* features in positive and negative ionization mode, with 267 and 344 *m/z* features detected in each mode, respectively. Of these *m/z* features, 330 were successfully assigned to a lipid identification, as listed in Supplementary Table S4 and S5. After subtracting different adducts and duplicates detected in both polarities, we assigned 280 unique lipid species. These lipids belonged to 25 distinct lipid classes. In positive ionization mode, these lipid classes were: sterols (ST), CE, Cer, PC, LPC, SM, DAG, and TAG. In negative ionization mode, we detected lipids from the following lipid classes: Cer, DCer, HexCer, LacCer, Cer 1-phosphates (CerP), Cer phosphoethanolamine (CerPE), Cer phosphoinositol (CerPI), FFA, monoacylglycerol (MG), phosphatidic acid (PA), PC (as $[M+Cl]^-$ ions) phosphoinositol (PI), PE, phosphatidylserine (PS), phosphatidylglycerol (PG), lysophosphoinositol (LPI), LPE, lysophosphatidylserine (LPS), lysophosphatidylglycerol (LPG) and SM (as $[M+Cl]^-$ ions). Lipid species belonging to the same lipid class often showed similar distributions, although interesting differences exist. Supplementary Fig. S1 shows the distribution of a representative lipid from every lipid class.

3.5. *Unsupervised clustering analysis extracts the major spectral patterns*

Using unsupervised NMF, we reduced the dimensionality of the spectral data by extracting the major spectral patterns. The positive ion mode data could be described in 8 components. The spatial distribution and mass spectrum of every component can be seen in Supplementary Fig. S3. All components consisted of mainly one or two lipid classes each. Component 1 was driven by mainly oxidized and non-oxidized CE species. The major CE species dominating the spectrum were CE(18:1) (cholesteryl oleate) and CE(18:2) (cholesteryl linoleate). Component 2

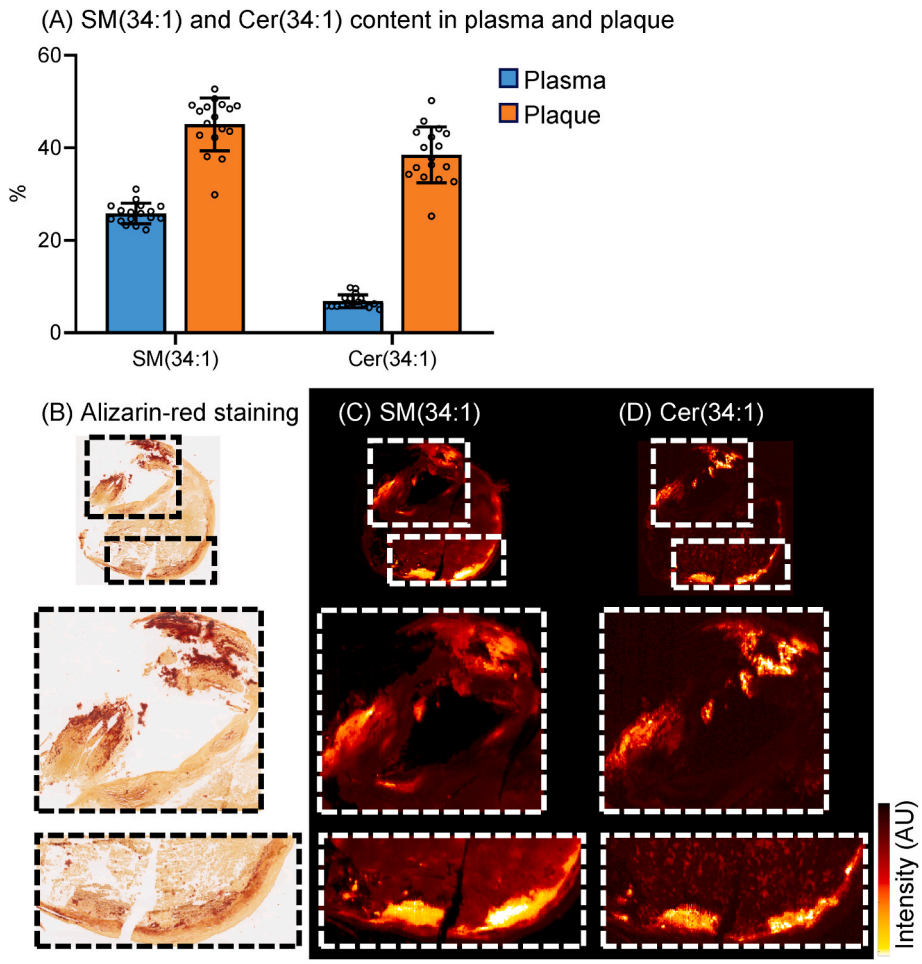

Fig. 3. Cer(34:1) accumulates in plaque and colocalizes with SM(34:1) and calcified plaque regions.
(A) Average (N = 17) SM(34:1) and Cer(34:1) content in plasma and plaque as a percentage of the total SM and Cer content. Error bars indicate the standard deviation, and individual data points of all samples are represented as circles. (B) Alizarin-Red S staining, the zoomed regions display the calcified regions; (C) DESI-MSI image (20 × 20 μm^2) of SM(34:1), with the zoomed regions colocalizing with calcified regions; (D) DESI-MSI image (20 × 20 μm^2) of Cer(34:1), with the zoomed regions colocalizing with calcified regions. (For interpretation of the references to colour in this figure legend, the reader is referred to the Web version of this article.)

was driven by TAG species. Component 3 was driven by a combination of SM and CE species. Component 4 was driven by a combination of CE and TAG species, where CE(18:2) was the most present. Component 5 was driven by SM species and, to a lesser extent, Cer species. Component 6 described the PC species and, to a smaller extent, the LPC species. Component 7 was dominated by cholesterol; this component also contained unknown peaks. Finally, component 8 consisted of CE species, mainly CE(18:1), and some PC species.

The negative ion mode data could be described by 5 components; see Supplementary Fig. S4 for the spatial distributions and mass spectra per component. Component 1 was driven by mainly one species, namely PI (38:4), and contained, to a lesser extent, a mix of other phospholipid species. Components 2 and 3 were driven by HexCer species, mainly by HexCer(34:1) and HexCer(38:2), respectively, and, to a lesser degree, Cer species. Lastly, components 4 and 5 were driven by Cer species, mainly one species for each component, Cer(34:1) and Cer(42:1), respectively.

3.6. Quantification of histology

We assessed and quantified the extent of positive staining in tissue samples for the following stains: CD68 Antibody, Alizarin-Red, MSB, ORO, ASMase, and ApoB. The relative proportions of each staining are detailed in Supplementary Table S5. We compared the patterns from CD68 Antibody, Alizarin-Red, and MSB stains with the lipid profiles obtained from DESI-MSI (details in subsequent sections). Notably, ASMase staining patterns were highly similar to those of CD68 antibody, thus eliminating the need for DESI-MSI comparisons. Additionally, ApoB staining was widespread across almost the entire plaque section, making it non-specific for lipid spectral pattern colocalization. Examples for ASMase and ApoB stains can be found in Supplementary Fig. S5.

3.7. Sphingomyelins and ceramides colocalize with each other and with calcified plaque regions

When comparing DESI-MSI spectral patterns with histology, we identified a colocalization of SM and Cer species with calcified plaque regions as determined by an Alizarin-Red S staining. Fig. 3B provides an example, illustrating the calcified regions alongside the distributions of SM(34:1) and Cer(34:1). This figure also reveals a marked difference in the intensity of SM(34:1) between the upper and lower parts of the plaque. In positive ionization mode, the species with the highest colocalization with the calcified plaque regions were SM(34:1) and Cer (34:1), with, on average, 54 % and 52 %, respectively, of the 10 % most intense pixels located in the calcified plaque region. This finding was confirmed in negative mode, where Cer(34:1) showed the highest colocalization (55 %) with calcified plaque regions and other Cer species. See Supplementary Table S7A and B for the complete list of lipids colocalizing with calcifications.

This data also suggest the colocalization of SM and Cer species,

which is confirmed by the NMF data. NMF component 3 of the positive ion data was driven by SMs and Cers. In negative mode, NMF component 4, largely driven by Cer(34:1), displayed a similar distribution as component 3 in the positive data. Interestingly, although ASMase is known to facilitate the conversion of SM to Cer, it was not localized in the same areas as SM and Cer but rather surrounding them, as depicted in Supplementary Fig. S5B and C. Additionally, low-density lipoprotein (LDL) particles can carry SMase activity. While our ApoB staining did reveal some overlap with areas rich in SM/Cer, as shown in Supplementary Fig. 5A and C, its widely spread distribution across the plaque indicates that this overlap is not specific for SM/Cer.

3.8. Phospholipids and free fatty acids colocalize with macrophage-infiltrated plaque regions

A comparison between histology and MSI data showed colocalization between the spectral pattern of phospholipids and FFAs and plaque areas high in inflammatory cells, such as macrophages, as stained by a CD68 antibody stain, see Fig. 4. Notably, the intensity of FFA(20:4) in Fig. 4C was less prominent as compared to regions A and B. In positive ionization mode, PCs (NMF component 6 of the positive data) colocalized with CD68 antibody-positive regions. On average, 43 % of the most intense DESI-MSI pixels of PC species colocalized with macrophage-infiltrated regions. PC species displayed a colocalization of 43 % of the most intense DESI-MSI with macrophage-infiltrated regions. Some species displaying the highest colocalization were PC(38:6) $[M+H]^+$ or PC(36:3) $[M+Na]^+$, PC(38:8) $[M+H]^+$,and PC(38:5) $[M+Na]^+$. In negative ionization mode, lipid species associated with CD68 positive regions were a mix of phospholipids and FFA species (NMF component 1 of the negative data). Phospholipids and all four detected FFAs displayed a colocalization of, on average, 43 % and 35 %, respectively, of the most intense DESI-MSI pixels with macrophage-infiltrated regions. These included PE(38:4), PI(O-34:3), and PS(40:6), and the FFAs, FFA(18:1), FFA(18:2), FFA(20:4), and FFA(22:4) (all detected as $[M-H]^-$ ions). See Supplementary Table S7 for the list of lipids colocalizing the most with CD68-positive plaque regions.

3.9. Triacylglycerols and phosphatidylinositols colocalize with areas rich in fibrin

As determined by the MSB staining, the plaque regions rich in the thrombus-associated coagulation protein fibrin were rich in TAG (NMF component 3 of the positive data) and PI species (see Fig. 5). The TAG species colocalizing the most with fibrin-rich areas, on average, 36 % of the most intense DESI-MSI pixels, were the polyunsaturated long-tail species TAG(58:8), TAG(58:9), and TAG(60:9) (all detected as $[M+Na]^+$ ions). The PI species colocalizing the most with fibrin-rich areas, that is, on average, 30 % of the most intense DESI-MSI pixels, were PI(36:1), PI(36:2), PI(34:1), and PI(38:3) (all detected as $[M-H]^-$ ions). See Supplementary Table S7 for the complete list of lipids colocalizing with fibrin.

4. Discussion

Lipids are a group of highly multifunctional molecules in the atherosclerotic disease process; they can act as signaling or initiating molecules, or be present as traces of plaque-forming mechanisms. Traditional lipidomics studies characterize this interplay by sampling the plasma lipid spectrum. Here, we studied the presence and location of lipids in atherosclerotic plaque to characterize their spatial distribution in the vessel wall and their association with plaque destabilization processes as seen in histology. In particular, we characterized lipids in three critical regions of plaque destabilization. Firstly, we focused on calcified regions, since spotty and superficial calcifications are indicators of plaque instability [26,27], and the progression of calcifications in coronary plaques has been significantly linked with increased mortality [28]. Secondly, we explored areas abundant in inflammatory cells. These cells play a prominent role in plaque destabilization by

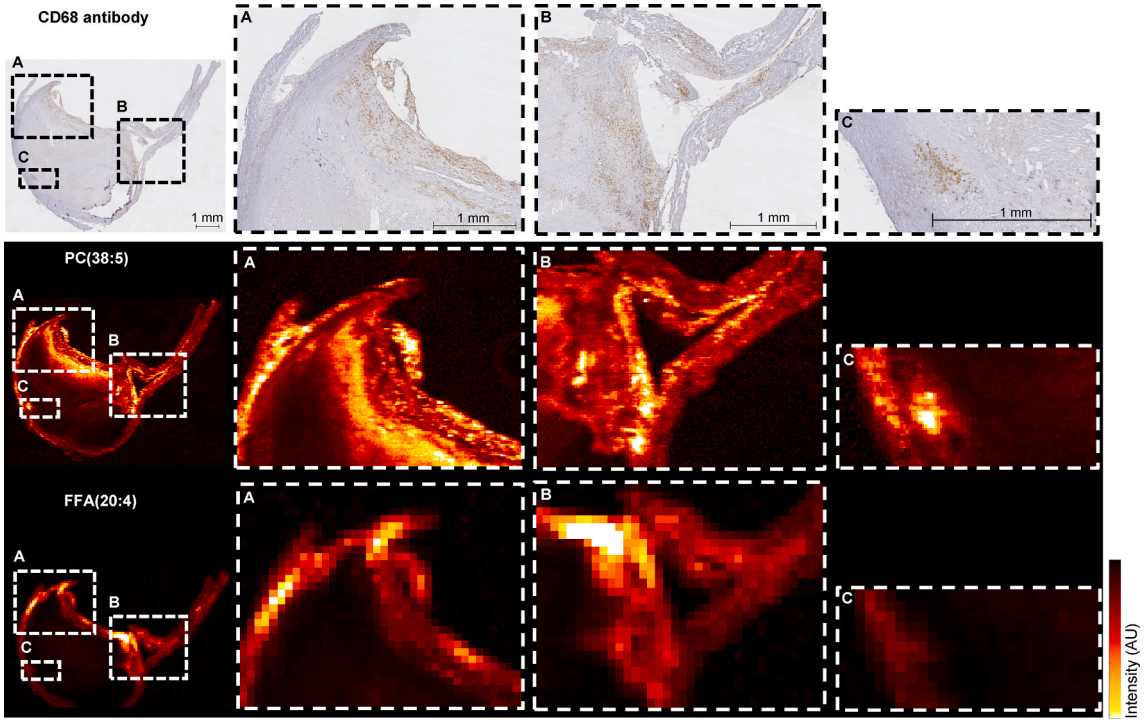

Fig. 4. PC and FFA species colocalize with plaque regions rich in macrophage infiltration.
(A–C) display the regions rich in macrophage infiltration shown in brown in the CD68 antibody stain, and the colocalizing regions of PC(38:5) $[M+Na]^+$ (20 × 20 μm^2) and FFA(20:4) $[M-H]^-$ (100 × 100 μm^2) in the DESI-MSI images. (For interpretation of the references to colour in this figure legend, the reader is referred to the Web version of this article.)

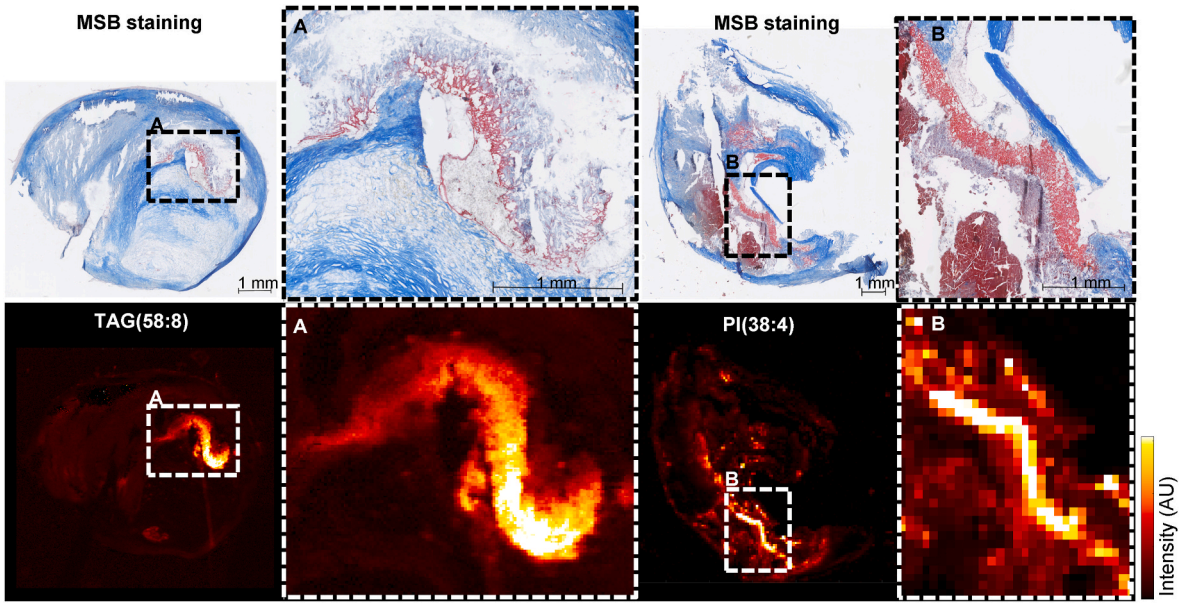

Fig. 5. TAG and PI colocalize with fibrin-rich plaque regions.
(A) MSB staining of a plaque with fibrin-rich regions in bright red and the colocalizing region of a DESI-MSI image (20 × 20 μm^2) of TAG(58:8) $[M+Na]^+$. (B) MSB staining of another plaque with a fibrin-rich region in bright red and the colocalizing DESI-MSI image (100 × 100 μm^2) of PI(38:4) $[M-H]^-$ in that plaque. (For interpretation of the references to colour in this figure legend, the reader is referred to the Web version of this article.)

weakening the fibrous cap [29], enlarging the necrotic core, and amplifying the inflammatory response [30]. Lastly, we incorporated regions rich in fibrin. Fibrin represents remnants of intra-plaque hemorrage, a consequence of neoangiogenesis within the plaque. This process leads to the formation of rupture-prone microvessels known to further exacerbate plaque instability [31,32]. To gain a comprehensive understanding, we also analyze plasma lipids in conjunction with their counterparts in plaque to locate salient circulating lipid species in plaque development. For this purpose, we performed lipidomics on carotid plaque and plasma samples from seventeen patients that underwent carotid endarterectomy.

To investigate the role of lipids in composition-related plaque instability, we used DESI-MSI to visualize lipid distributions in tissue sections from fourteen carotid plaques. We compared lipid distributions to plaque areas of interest as defined by histology. We detected 611 lipid-related *m/z* features, of which 330 could be assigned to a lipid identification. Annotated lipids belonged to 25 different lipid classes. Unsupervised NMF clustering revealed patterns largely dominated by one or two lipid classes per component in both positive and negative mode. Colocalization of a few specific components with identifiable pathologic features on histology supported the identification of highly abundant lipids in these areas, for instance, positive ion mode NMF 3 and negative ion mode NMF 4 with calcifications and positive ion mode NMF 6 with inflammation.

Plasma lipidomics can provide individualized risk assessment. However, the mechanisms linking plasma lipids to elevated cardiovascular risk still need to be discovered. Our study locates prominent plasma lipids in plaque and recognizes plaque formation processes that coexist with these lipids. Lipids can interact with plaque either by the deposition of circulating species or by shedding lipids by plaque. In the former, lipids produced in systemic metabolism may enter the circulation and be deposited in plaque through leaky vasa vasorum, dysfunctional endothelium, or lipoprotein deposition [33–35]. These lipids may then drive plaque development by stimulating inflammation, (micro-) calcification, and other mechanisms [36]. In the latter, plaque lipid species may migrate into the bloodstream through the release of extracellular vesicles containing intracellular lipids [37,38], via leaky vasa vasorum [35] or (asymptomatic) plaque ulceration or rupture releasing extracellular plaque lipids into the bloodstream. Through these mechanisms, lipids that originate in plaques may be released into the blood, albeit in very small quantities which renders the possibility of their detection uncertain. Several enzymatic processes convert lipids in the course of plaque development, creating specific molecular species that are enriched in plaque.

Lipidomics showed differences in lipid class composition between plasma and plaque samples. As expected, both plasma and plaque samples consisted for a large part of CEs, with cholesteryl oleate and cholesteryl linoleate being the most prominent species. In contrast to plasma, plaque exhibited a higher proportion of cholesteryl oleate than cholesteryl linoleate, which is consistent with previous research findings [39]. Although both species are considered pro-atherogenic, cholesteryl oleate is considered more pro-atherogenic compared to cholesteryl linoleate by forming a more crystalline structure within the plaque [40] making it more rigid and prone to rupture [41]. Additionally, plasma CEs accounted for 37 % of the total lipid content, whereas in plaque, this was increased to 63 %. The relatively higher CE content in plaque compared to plasma can be explained by the transformation of cholesterol to CE by enzymatic activity in the vessel wall. CEs tend to accumulate in macrophages and smooth muscle cells, which leads to foam cell formation, and thus plaque formation and growth [42]. Similar differences exist between plaque and plasma for other lipid classes.

On an individual lipid species level, we found several molecular lipid species that were significantly different between plasma and plaque (VIP >1.0), resulting from the OPLS-DA model comparing plasma to plaque. We focussed on the significantly different lipids with which plaques were enriched, which could elucidate what lipids are accumulating in the vessel wall or actively produced in the plaque. Among these plaque-enriched species were several FFA species. Previous research described a positive association between increased FFA plasma levels and cardiovascular risk [43]. FFAs play a role in the development of atherosclerosis by impeding endothelium-dependent vasodilation, inducing monocyte adhesion to endothelial cells, and promoting inflammation in the vascular wall [44–46]. FFA(16:0) and FFA(18:1) were the most prevalent FFA species in both plasma and plaque, however, relatively more FFA(16:0) is accumulating in plaque. This is of interest, because saturated fatty acids, such as FFA(16:0), or palmitic acid, have been

associated with inflammation and endothelial dysfunction [47]. DESI-MSI visualized the spatial pattern of four FFAs; these were FFA (18:1), FFA(18:2), FFA(20:4), and FFA(22:4). All four FFA species were located in plaque areas rich in macrophage-infiltration, which corroborates their role in inflammatory processes. As illustrated in Fig. 4, the intensity of FFA(20:4) was notably less dominant in area C than in areas A and B. This variation might be due to heterogeneity among macrophages within the plaque microenvironment. Specifically, area C was characterized by a discrete cluster of macrophages located at the outer border of the plaque. This patters suggests that these macrophages in area C may represent a distinct subset, possibly identified as intralesional macrophages. In contrast, macrophages closer to the lumen or in the shoulder region of the plaque (area A and B) seemed to align more with the typical fibrous cap macrophages.

Though most PC species were relatively more present in plasma, two species, namely PC(32:0) and PC(34:1), were relatively enriched in plaque. Previous research has found an association between PC(32:0) and fibroblast cell growth [48]. Fibroblasts play a role in atherosclerotic plaque progression by regulating inflammation, producing collagen, and preserving plaque structure [49,50]. Furthermore, the combination of PC(32:0) plasma levels and six other PC and Cer species was proposed as a novel risk score for cardiovascular death in coronary artery disease patients [51]. A vascular lipidomics study in atherosclerotic mice demonstrated an increase of certain PC species, including PC(34:1), in the plaque of mice on a high-fat diet compared to mice on a normal diet [52].

When looking at the spatial patterns of PCs in plaque, we found a colocalization with plaque regions rich in macrophage infiltration. This colocalization can be explained by the upregulation of PC biosynthesis in the cell membrane of lesional macrophages, leading to an increase in PC mass. The upregulation of PC biosynthesis is thought to be a response to the accumulation of free cholesterol in the macrophages, which can reach cytotoxic levels. A healthy PC/free cholesterol ratio in the cell membrane prevents cytotoxicity and subsequent cell death [53–55]. Different subpopulations of macrophages can occur in plaque, with different degrees of pro-inflammatory properties. Oxidized PC species, which we also detected in macrophage-rich regions, induce polarization of macrophages to the Mox phenotype in mice. Mox macrophages have a decreased phagocytotic capacity which may contribute to tissue damage and pro-inflammatory processes leading to the destabilization of plaques [56].

The interacting processes of lipid accumulation and inflammation are important drivers of plaque growth and destabilization [2,57]. CE-rich Apo-B100 apolipoproteins have been related to inflammatory activity in human carotid specimens [58], further detailing the transport mechanism underlying the NLRP3 inflammasome activation by cholesterol crystals. Above, we discussed the colocalization of inflammation, as seen through macrophage proliferation, and specific lipids (FFAs and PCs). We also stained for ApoB in our study. However, ApoB was widespread across almost the entire tissue in these advanced plaques, preventing any specific colocalization with distinct lipid spectral patterns. Thus, even though there is a potential spatial relationship between the distributions of FFAs, PCs, and apolipoproteins — given that LDL or very-low-density lipoprotein (VLDL) particles containing these lipids can deposit them — the prevalence of ApoB staining in our samples made it challenging to draw definitive conclusions in this context. It's worth noting that FFAs and PCs have multiple origins, including local synthesis and degradation processes that operate independently of apolipoprotein deposition. Consequently, there may be regions where these lipid species are detected without corresponding apolipoprotein presence.

SM and Cer species showed similar spatial patterns located close to the outer vessel wall. This can be seen from the similar NMF patterns of component 3 in positive mode containing SM and Cer species and NMF component 3 in negative mode containing Cer species. As described in the lipidomics data, SM(34:1) and Cer(34:1) constituted most of the SM and Cer content of plaque. Interestingly, Cer(34:1) was identified as the lipid with the highest associated risk for cardiovascular events in plasma lipidomics studies [5]. This species is relatively scarce in plasma but is a prominent lipid in the advanced plaques we study here. Notably, previous research has found that the sphingolipid signaling pathway is enriched in human carotid plaque, further underscoring the importance of these lipids in plaque formation [19]. The observed colocalization of SM and Cer species and the increased Cer(34:1) content in plaque, but not in plasma, is sphingomyelinase (SMase) enzyme activity in the vessel wall [59,60]. SMase activity is deposited from sources including LDL particles and can hydrolyze SMs into Cers and phosphorylcholine [61,62]. In line with this work, Schissel et al. have found a SMase-induced 10–50 fold increase of Cers in aggregated LDL particles in atherosclerotic plaque compared to plasma LDL Cers [60]. The high particle Cer content of these aggregated LDL particles catalyzes further aggregation of LDL particles by promoting LDL-LDL interactions and, thus, plaque growth. We conducted an ApoB staining to detect LDL presence. While this staining revealed areas overlapping with regions abundant in SM and Cer, it was also widely distributed across the plaque, making it non-specific to just the SM/Cer-rich areas.

Furthermore, we described a colocalization between the spatial pattern of SMs and Cers with the calcified plaque regions, as defined by an Alizarin Red staining. In Fig. 3B and C, a differential intensity of SM (34:1) between the upper and lower parts of the plaque was observed, a distinction that can be linked to the different stages of calcifications present within these regions. Notably, the pronounced staining in the upper part signifies the presence of macro-calcifications, whereas the lower part with less prominent staining reflects the presence of micro-calcifications, which represent initial calcification stages. This observation aligns well with SMase activity, represented by SM(34:1) and Cer (34:1), which can facilitate the transformation of vascular smooth muscle cells (VSMCs) into an osteogenic cell type. It is plausible to anticipate higher levels of SM(34:1) in regions where active calcification is taking place. Neutral and ASMase-derived Cers play a crucial role in the phenotypic switch of VSMCs to an osteo-chondrogenic phenotype which can calcify tissue through mechanisms similar to bone formation [11,63]. Living, but also apoptotic, transdifferentiated VSMCs secrete exosomes containing enzymes and lipids that stimulate the formation of solid calcium deposits such as PS and calcium-binding proteins [64]. Inhibiting the ASMase activity attenuated vascular calcification in mice, and *ex vivo* isolated perfused arteries [63]. Moreover, mice with SMC-specific overexpression of the ASMase gene were found to have increased aortic and coronary medial calcification [65]. In our investigation, ASMase staining showed a distribution pattern similar to that of CD68, surrounding the calcified plaque areas rather than being located within the same regions of calcification, SMs, and Cers. The observed similarity with macrophages is expected, given that they are the primary source of ASMase within plaques [66]. The relationship between ASMase and plaque development may be complex and could be influenced by temporal factors. For instance, during an earlier phase of plaque development, ASMase might have played a more direct role in Cer production in the calcified area. By the time of our observations, ASMase may have already exerted its effects and moved to neighboring regions to continue its biological activities.

We identify an increased abundance of PI in regions with intraplaque hemorrhage and subsequent thrombus formation, which can be identified in histology by their fibrin content. PI compounds, specifically PI 4,5-biphosphate and PI 3-monophosphate, activate several key proteins involved in the blood coagulation pathway, such as platelet phospholipase C [67–69]. Previous research has found TAGs surrounding neovessels within plaque [14], potentially related to intra-plaque hemorrhage and the subsequent fibrin formation. This study corroborates the previously reported [18] association between TAG and fibrin-rich plaque regions. Relative to MALDI studies, we find a smaller DAG content in fibrin-rich areas, suggesting that part of the DAGs observed earlier may result from TAG fragmentation. One plaque in our

dataset had no colocalization of fibrin with TAG or PI species but with PC species. Further examination of the histology of this sample suggests that this lack of colocalization with TAG and PI may be attributed to its fibrin content that is not associated with intra-plaque hemorrhage but rather with a mural thrombus fragment, see Fig. S6.

To our knowledge, this is the first study combining plaque and plasma lipidomics with dual-polarity DESI-MSI for detailed lipid characterization of human carotid atherosclerotic plaque. Furthermore, we could correlate specific lipid species to histologically-defined plaque areas of interest by performing histology on consecutive tissue sections. Compared to earlier MSI studies of human atherosclerotic plaque, we detected more distinct lipids and could identify a larger fraction. The larger number of lipid species also produced a more finely-grained clustering analysis, which means that not all of these patterns could be matched to known features from histology.

4.1. Limitations

The sample size of our study is relatively small, which could affect the generalizability of our findings. Furthermore, all patients in this study were on lipid-lowering medications, which may limit the conclusions that can be drawn from our data for the general population. Additionally, we used one 3 mm cross-section of each plaque for tissue lipidomics and one section per plaque for DESI-MSI; this may not fully capture the heterogeneity of each sample. Further research on a larger sample size would be necessary to confirm our findings.

DAG(40:0) constituted 65 % of the total DAG content in plaque, while in plasma, it constituted less than 1 %. No previous research has described a relation between DAG(40:0) and atherosclerotic plaque. Despite DAG(40:0) being the most prominent DAG species in plaque, we did not detect this lipid in plaque with DESI-MSI. Since DAG(40:0) is a relatively unknown lipid and no specific internal standard for DAG (40:0) was included, we cannot verify its identification.

Lipids detected with DESI-MSI were annotated based on their exact mass and guided by common lipid patterns as expected in mammal biology. Due to the large number of lipid species detected, we did not use MS/MS to annotate detected peaks. MS/MS provides more structural information, which would be necessary to identify isobaric species and distinguish structural isomers. An example related to this limitation was HexCer species and odd chained PS species, which have almost identical masses, and, thus, cannot be assigned with confidence based on exact mass. Since lipid species with odd carbon chain lengths are rare in mammalian tissue, we decided to discard the odd chained PS annotations. However, some studies reported the presence of PS species with an odd chain length in mammalian tissues, which suggests that they may occasionally be present [52,70]. Furthermore, in negative ionization mode, chloride adducts can be formed from two stable chlorine isotopes ^{35}Cl and ^{37}Cl. This results in, for instance, Cer(34:1) $[M+^{35}Cl]^-$ having an almost identical mass as Cer(34:2) $[M+^{37}Cl]^-$. Because the chlorine adduct formation occurs from naturally occurring chlorine in the biological sample, and the natural isotope distribution pattern of chlorine is $^{35}Cl/^{37}Cl$ ~3/1, we choose only to report ^{35}Cl adducts. Similarly, different chain length, saturation, and adduct ($+Na^+/+H^+$) combinations were possible in the assignment of PCs we observed. We chose to report only those species in the DESI analysis that were detected in the plaque lipidomics data.

4.2. Conclusion

We analyzed a heterogeneous data set comprising lipidomic analyses of plasma and plaque from patients undergoing carotid endarterectomy. By comparing the lipid species in plaque and plasma, we identified those circulating species that accumulate prominently in plaque. Quantitative comparison of lipid spectral patterns with histology revealed the

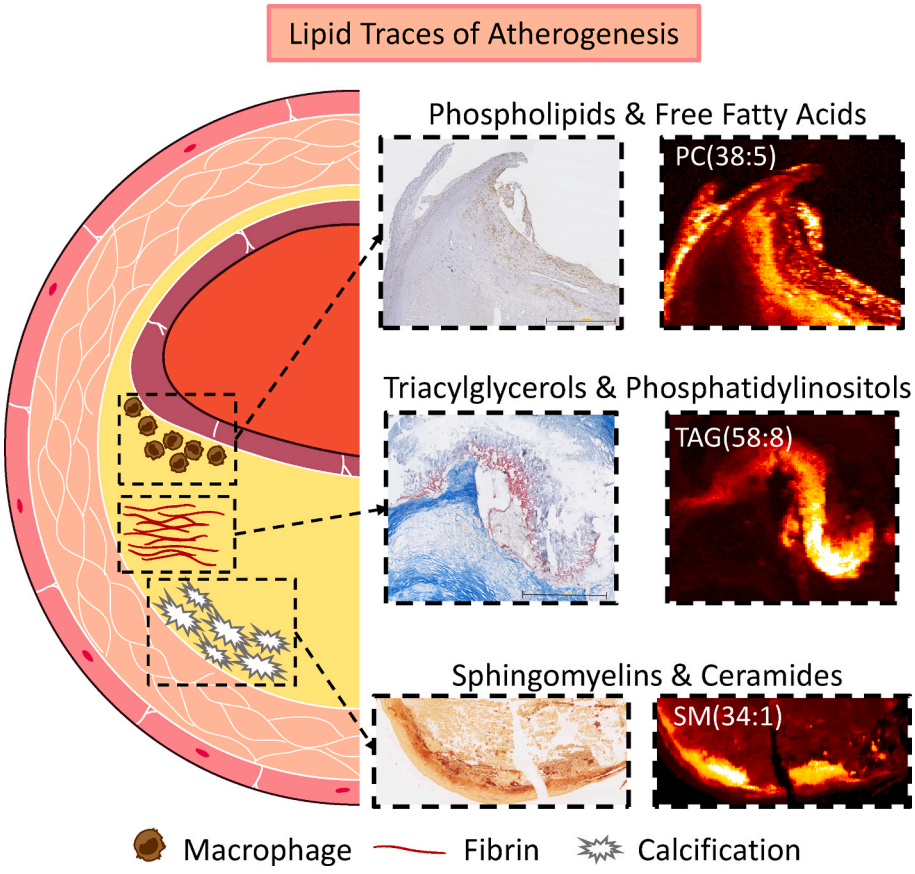

Fig. 6. Graphical abstract illustrating the presence of lipid species in plaque areas associated with destabilization processes.

presence of lipid species in areas of plaque associated with destabilization processes (Fig. 6), corroborating previous *in vitro* and animal studies. Specifically, calcified areas exhibited a high abundance of SM and Cer, while macrophage infiltration was associated with phospholipids and FFA. In regions rich in fibrin, indicative of intra-plaque hemorrhage, we observed TAG and PI species.

Financial support

This study was funded by NWO Vici 16131.

CRediT authorship contribution statement

Nuria Slijkhuis: Conceptualization, Investigation, Validation, Data curation, Formal analysis, Methodology, Writing – original draft, Writing – review & editing. **Mark Towers:** Data curation, Investigation, Methodology, Writing – review & editing. **Mina Mirzaian:** Data curation, Investigation, Methodology, Writing – review & editing. **Suze-Anne Korteland:** Formal analysis, Software, Methodology, Writing – review & editing. **Bram Heijs:** Data curation, Methodology, Writing – review & editing. **Kim van Gaalen:** Data curation, Investigation, Methodology, Writing – review & editing. **Ingeborg Nieuwenhuizen:** Data curation, Investigation, Methodology, Writing – review & editing. **Alex Nigg:** Software, Methodology, Writing – review & editing. **Kim van der Heiden:** Resources, Methodology, Writing – review & editing. **Yolanda B. de Rijke:** Resources, Project administration, Methodology, Writing – review & editing. **Aad van der Lugt:** Resources, Project administration, Methodology, Writing – review & editing. **Eric J.G. Sijbrands:** Conceptualization, Methodology, Validation, Writing – review & editing. **Emmanuelle Claude:** Data curation, Investigation, Methodology, Writing – review & editing. **Gijs van Soest:** Conceptualization, Project administration, Validation, Methodology, Resources, Supervision, Writing – review & editing, Funding acquisition.

Declaration of competing interest

The authors declare the following financial interests/personal relationships which may be considered as potential competing interests: Mark Towers and Emmanuelle Claude are employees of Waters Corporation. The other authors have no conflicts of interest to disclose.

Acknowledgments

The graphical abstract was partly generated using Servier Medical Art, licensed under Creative Commons Attribution 3.0 unported license.

Appendix A. Supplementary data

Supplementary data to this article can be found online at https://doi.org/10.1016/j.atherosclerosis.2023.117340.

References

[1] G.B.D. Collaborators, Global, regional, and national age-sex specific mortality for 264 causes of death, 1980-2016: a systematic analysis for the Global Burden of Disease Study 2016, Lancet 390 (2017) 1151–1210, https://doi.org/10.1016/S0140-6736(17)32152-9.

[2] R. Ross, Atherosclerosis — an inflammatory disease, N. Engl. J. Med. 340 (1999) 115–126, https://doi.org/10.1056/nejm199901143400207.

[3] M.C. Fishbein, The vulnerable and unstable atherosclerotic plaque, Cardiovasc. Pathol. 19 (2010) 6–11, https://doi.org/10.1016/j.carpath.2008.08.004.

[4] M. Naghavi, P. Libby, E. Falk, S.W. Casscells, S. Litovsky, J. Rumberger, J. J. Badimon, C. Stefanadis, P. Moreno, G. Pasterkamp, et al., From vulnerable plaque to vulnerable patient: a call for new definitions and risk assessment strategies: Part I, Circulation 108 (2003) 1664–1672, https://doi.org/10.1161/01.CIR.0000087480.94275.97108/14/1664.

[5] J.M. Cheng, M. Suoniemi, I. Kardys, T. Vihervaara, S.P.M. de Boer, K.M. Akkerhuis, M. Sysi-Aho, K. Ekroos, H.M. Garcia-Garcia, R.M. Oemrawsingh, et al., Plasma concentrations of molecular lipid species in relation to coronary plaque characteristics and cardiovascular outcome: results of the ATHEROREMO-IVUS study, Atherosclerosis 243 (2015) 560–566, https://doi.org/10.1016/j.atherosclerosis.2015.10.022.

[6] C. Stegemann, R. Pechlaner, P. Willeit, S.R. Langley, M. Mangino, U. Mayr, C. Menni, A. Moayyeri, P. Santer, G. Rungger, et al., Lipidomics profiling and risk of cardiovascular disease in the prospective population-based bruneck study, Circulation 129 (2014) 1821–1831, https://doi.org/10.1161/circulationaha.113.002500.

[7] P. Duewell, H. Kono, K.J. Rayner, C.M. Sirois, G. Vladimer, F.G. Bauernfeind, G. S. Abela, L. Franchi, G. Nuñez, M. Schnurr, et al., NLRP3 inflammasomes are required for atherogenesis and activated by cholesterol crystals, Nature 464 (2010) 1357–1361, https://doi.org/10.1038/nature08938.

[8] K. Rajamäki, J. Lappalainen, K. Öörni, E. Välimäki, S. Matikainen, P.T. Kovanen, K. K. Eklund, Cholesterol crystals activate the NLRP3 inflammasome in human macrophages: a novel link between cholesterol metabolism and inflammation, PLoS One 5 (2010), e11765, https://doi.org/10.1371/journal.pone.0011765.

[9] Z. Li, M.J. Basterr, T.K. Hailemariam, M.R. Hojjati, S. Lu, J. Liu, R. Liu, H. Zhou, X. C. Jiang, The effect of dietary sphingolipids on plasma sphingomyelin metabolism and atherosclerosis, Biochim. Biophys. Acta 1735 (2005) 130–134, https://doi.org/10.1016/j.bbalip.2005.05.004.

[10] T.S. Park, R.L. Panek, S.B. Mueller, J.C. Hanselman, W.S. Rosebury, A. W. Robertson, E.K. Kindt, R. Homan, S.K. Karathanasis, M.D. Rekhter, Inhibition of sphingomyelin synthesis reduces atherogenesis in apolipoprotein E-knockout mice, Circulation 110 (2004) 3465–3471, https://doi.org/10.1161/01.CIR.0000148370.60535.22.

[11] L. Liao, Q. Zhou, Y. Song, W. Wu, H. Yu, S. Wang, Y. Chen, M. Ye, L. Lu, Ceramide mediates Ox-LDL-induced human vascular smooth muscle cell calcification via p38 mitogen-activated protein kinase signaling, PLoS One 8 (2013), e82379, https://doi.org/10.1371/journal.pone.0082379.

[12] J. Andrew, E.L.M. Brown, Ingrid C. Gelissen, Kritharides Leonard, Roger T. Dean, Wendy Jessup. Cholesterol and oxysterol metabolism and subcellular distribution in macrophage foam cells: accumulation of oxidized esters in lysosomes, JLR (J. Lipid Res.) 41 (2000) 226–236, https://doi.org/10.1016/S0022-2275(20)32056-3.

[13] K. Chughtai, R.M. Heeren, Mass spectrometric imaging for biomedical tissue analysis, Chem. Rev. 110 (2010) 3237–3277, https://doi.org/10.1021/cr100012c.

[14] S. Lehti, P. Sjövall, R. Käkelä, M.I. Mäyränpää, P.T. Kovanen, K. Öörni, Spatial distributions of lipids in atherosclerosis of human coronary arteries studied by time-of-flight secondary ion mass spectrometry, Am. J. Pathol. 185 (2015) 1216–1233, https://doi.org/10.1016/j.ajpath.2015.01.026.

[15] J. Cao, P. Goossens, M. Martin-Lorenzo, F. Dewez, B.S.R. Claes, E.A.L. Biessen, R.M. A. Heeren, B. Balluff, Atheroma-specific lipids in ldlr(-/-) and apoe(-/-) mice using 2D and 3D matrix-assisted laser desorption/ionization mass spectrometry imaging, J. Am. Soc. Mass Spectrom. 31 (2020) 1825–1832, https://doi.org/10.1021/jasms.0c00070.

[16] N. Zaima, T. Sasaki, H. Tanaka, X.W. Cheng, K. Onoue, T. Hayasaka, N. Goto-Inoue, H. Enomoto, N. Unno, M. Kuzuya, et al., Imaging mass spectrometry-based histopathologic examination of atherosclerotic lesions, Atherosclerosis 217 (2011) 427–432, https://doi.org/10.1016/j.atherosclerosis.2011.03.044.

[17] F. Greco, L. Quercioli, A. Pucci, S. Rocchiccioli, M. Ferrari, F.A. Recchia, L. A. McDonnell, Mass spectrometry imaging as a tool to investigate region specific lipid alterations in symptomatic human carotid atherosclerotic plaques, Metabolites 11 (2021), https://doi.org/10.3390/metabo11040250.

[18] A.M. Moerman, M. Visscher, N. Slijkhuis, K. Van Gaalen, B. Heijs, T. Klein, P. C. Burgers, Y.B. De Rijke, H.M.M. Van Beusekom, T.M. Luider, et al., Lipid signature of advanced human carotid atherosclerosis assessed by mass spectrometry imaging, J. Lipid Res. 62 (2021), 100020, https://doi.org/10.1194/jlr.RA120000974.

[19] W. Li, J. Luo, F. Peng, R. Liu, X. Bai, T. Wang, X. Zhang, J. Zhu, X.Y. Li, Z. Wang, et al., Spatial metabolomics identifies lipid profiles of human carotid atherosclerosis, Atherosclerosis 364 (2023) 20–28, https://doi.org/10.1016/j.atherosclerosis.2022.11.019.

[20] N.E. Manicke, M. Nefliu, W. Chunping, J.W. Woods, V. Reiser, R.C. Hendrickson, R. G. Cooks, Imaging of lipids in atheroma by desorption electrospray ionization mass spectrometry, Anal. Chem. 81 (2009) 8702–8707, https://doi.org/10.1021/ac901739s.

[21] M. Visscher, A.M. Moerman, P.C. Burgers, H.M.M. Van Beusekom, T.M. Luider, H. J.M. Verhagen, A.F.W. Van der Steen, K. Van der Heiden, G. Van Soest, Data processing pipeline for lipid profiling of carotid atherosclerotic plaque with mass spectrometry imaging, J. Am. Soc. Mass Spectrom. (2019), https://doi.org/10.1007/s13361-019-02254-y.

[22] M. Strohalm, M. Hassman, B. Košata, M. Kodíček, mMass data miner: an open source alternative for mass spectrometric data analysis, Rapid Commun. Mass Spectrom. 22 (2008) 905–908, https://doi.org/10.1002/rcm.3444.

[23] The LIPID MAPS® Lipidomics Gateway. https://www.lipidmaps.org/.

[24] N. Verbeeck, R.M. Caprioli, R. Van De Plas, Unsupervised machine learning for exploratory data analysis in imaging mass spectrometry, Mass Spectrom. Rev. (2019) 1–47, https://doi.org/10.1002/mas.21602.

[25] Y. Li, A. Ngom, The non-negative matrix factorization toolbox for biological data mining, Source Code Biol. Med. 8 (2013), https://doi.org/10.1186/1751-0473-8-10, 10-10.

[26] Y. Vengrenyuk, S. Carlier, S. Xanthos, L. Cardoso, P. Ganatos, R. Virmani, S. Einav, L. Gilchrist, S. Weinbaum, A hypothesis for vulnerable plaque rupture due to stress-induced debonding around cellular microcalcifications in thin fibrous caps, Proc. Natl. Acad. Sci. USA 103 (2006) 14678–14683, https://doi.org/10.1073/pnas.0606310103.

[27] S. Ehara, Y. Kobayashi, M. Yoshiyama, K. Shimada, Y. Shimada, D. Fukuda, Y. Nakamura, H. Yamashita, H. Yamagishi, K. Takeuchi, et al., Spotty calcification

typifies the culprit plaque in patients with acute myocardial infarction: an intravascular ultrasound study, Circulation 110 (2004) 3424–3429, https://doi.org/10.1161/01.CIR.0000148131.41425.E9.
[28] M.J. Budoff, J.E. Hokanson, K. Nasir, L.J. Shaw, G.L. Kinney, D. Chow, D. Demoss, V. Nuguri, V. Nabavi, R. Ratakonda, et al., Progression of coronary artery calcium predicts all-cause mortality, JACC Cardiovasc Imaging 3 (2010) 1229–1236, https://doi.org/10.1016/j.jcmg.2010.08.018.
[29] A.C. Newby, Metalloproteinases and vulnerable atherosclerotic plaques, Trends Cardiovasc. Med. 17 (2007) 253–258, https://doi.org/10.1016/j.tcm.2007.09.001.
[30] I. Tabas, Macrophage death and defective inflammation resolution in atherosclerosis, Nat. Rev. Immunol. 10 (2010) 36–46, https://doi.org/10.1038/nri2675.
[31] P.R. Moreno, K.R. Purushothaman, V. Fuster, D. Echeverri, H. Truszczynska, S. K. Sharma, J.J. Badimon, W.N. O'Connor, Plaque neovascularization is increased in ruptured atherosclerotic lesions of human aorta: implications for plaque vulnerability, Circulation 110 (2004) 2032–2038, https://doi.org/10.1161/01.Cir.0000143233.87854.23.
[32] B.J. Dunmore, M.J. McCarthy, A.R. Naylor, N.P. Brindle, Carotid plaque instability and ischemic symptoms are linked to immaturity of microvessels within plaques, J. Vasc. Surg. 45 (2007) 155–159, https://doi.org/10.1016/j.jvs.2006.08.072.
[33] M.F. Linton, P.G. Yancey, S.S. Davies, W.G. Jerome, E.F. Linton, W.L. Song, A. C. Doran, K.C. Vickers, The Role of Lipids and Lipoproteins in Atherosclerosis, MDText.com, Inc., 2000.
[34] J.R. Guyton Kfk, B.L. Black, T.M.A. Bocani, Extracellular lipid deposition in atherosclerosis, Eur. Heart J. 11 (1990) 20–28.
[35] R. Virmani, F.D. Kolodgie, A.P. Burke, A.V. Finn, H.K. Gold, T.N. Tulenko, S. P. Wrenn, J. Narula, Atherosclerotic plaque progression and vulnerability to rupture: angiogenesis as a source of intraplaque hemorrhage, Arterioscler. Thromb. Vasc. Biol. 25 (2005) 2054–2061, https://doi.org/10.1161/01.ATV.0000178991.71605.18.
[36] C.V. Felton, D. Crook, M.J. Davies, M.F. Oliver, Relation of plaque lipid composition and morphology to the stability of human aortic plaques, Arterioscler. Thromb. Vasc. Biol. 17 (1997) 1337–1345, https://doi.org/10.1161/01.Atv.17.7.1337.
[37] N. Timmerman, F. Waissi, M. Dekker, G.J. de Borst, J. van Bennekom, R.J. de Winter, M. Hilvo, A. Jylha, G. Pasterkamp, D.P.V. de Kleijn, et al., Ceramides and phospholipids in plasma extracellular vesicles are associated with high risk of major cardiovascular events after carotid endarterectomy, Sci. Rep. 12 (2022) 5521, https://doi.org/10.1038/s41598-022-09225-6.
[38] C.M. Boulanger, X. Loyer, P.E. Rautou, N. Amabile, Extracellular vesicles in coronary artery disease, Nat. Rev. Cardiol. 14 (2017) 259–272, https://doi.org/10.1038/nrcardio.2017.7, doi: nrcardio.2017.7 [pii].
[39] C. Stegemann, I. Drozdov, J. Shalhoub, J. Humphries, C. Ladroue, A. Didangelos, M. Baumert, M. Allen, A.H. Davies, C. Monaco, et al., Comparative lipidomics profiling of human atherosclerotic plaques, Circulation: Cardiovascular Genetics 4 (2011) 232–242, https://doi.org/10.1161/circgenetics.110.959098.
[40] D.M. Small, Progression and regression of atherosclerotic lesions. Insights from lipid physical biochemistry, Arteriosclerosis: An Official Journal of the American Heart Association, Inc. 8 (1988) 103–129, https://doi.org/10.1161/01.Atv.8.2.103.
[41] M. John Chapman, R. Preston Mason, Cholesterol crystals and atherosclerotic plaque instability: therapeutic potential of Eicosapentaenoic acid, Pharmacol. Ther. 240 (2022), 108237, https://doi.org/10.1016/j.pharmthera.2022.108237.
[42] D.K.H. Jun Kusunoki, Katsumi Aragane, John T. Fallon, Juan J. Badimon, Edward A. Fisher, Acyl-CoA:Cholesterol acyltransferase inhibition reduces atherosclerosis in apolipoprotein E–deficient mice, Circulation 103 (2001) 2604–2609.
[43] M.H. Zhang, Y.X. Cao, L.G. Wu, N. Guo, B.J. Hou, L.J. Sun, Y.L. Guo, N.Q. Wu, Q. Dong, J.J. Li, Association of plasma free fatty acids levels with the presence and severity of coronary and carotid atherosclerotic plaque in patients with type 2 diabetes mellitus, BMC Endocr. Disord. 20 (2020) 156.
[44] H.O. Steinberg, M. Tarshoby, R. Monestel, G. Hook, J. Cronin, A. Johnson, B. Bayazeed, A.D. Baron, Elevated circulating free fatty acid levels impair endothelium-dependent vasodilation, J. Clin. Invest. 100 (1997) 1230–1239, https://doi.org/10.1172/JCI119636.
[45] W.Y. Zhang, E. Schwartz, Y. Wang, J. Attrep, Z. Li, P. Reaven, Elevated concentrations of nonesterified fatty acids increase monocyte expression of CD11b and adhesion to endothelial cells, Arterioscler. Thromb. Vasc. Biol. 26 (2006) 514–519, https://doi.org/10.1161/01.ATV.0000200226.53994.09.
[46] G. Boden, Free fatty acids, A major link between obesity, insulin resistance, inflammation, and atherosclerotic vascular, in: V.A. Fonseca (Ed.), Cardiovascular Endocrinology: Shared Pathways and Clinical Crossroads, Humana Press, 2009, pp. 61–70.
[47] J.Y. Lee, K.H. Sohn, S.H. Rhee, D. Hwang, Saturated fatty acids, but not unsaturated fatty acids, induce the expression of cyclooxygenase-2 mediated through Toll-like receptor 4, J. Biol. Chem. 276 (2001) 16683–16689, https://doi.org/10.1074/jbc.M011695200.
[48] H. Liu, J. Cao, B. Balluff, A. Jongen, M.J. Gijbels, J. Melenhorst, R.M.A. Heeren, N. D. Bouvy, Examination of lipid profiles in abdominal fascial healing using MALDI-TOF to identify potential therapeutic targets, J Mass Spectrom Adv Clin Lab 20 (2021) 35–41, https://doi.org/10.1016/j.jmsacl.2021.06.002.
[49] S. Singh, M. Torzewski, Fibroblasts and their pathological functions in the fibrosis of aortic valve sclerosis and atherosclerosis, Biomolecules 9 (2019), https://doi.org/10.3390/biom9090472.
[50] K. Tadeja, S.-Š. Snežna, The role of fibroblasts in atherosclerosis progression, in: B. Mojca Frank, L. Katja (Eds.), Fibroblasts, IntechOpen, Rijeka, 2021. Ch. 3.
[51] M. Hilvo, P.J. Meikle, E.R. Pedersen, G.S. Tell, I. Dhar, H. Brenner, B. Schöttker, M. Lääperi, D. Kauhanen, K.M. Koistinen, et al., Development and validation of a ceramide- and phospholipid-based cardiovascular risk estimation score for coronary artery disease patients, Eur. Heart J. (2019), https://doi.org/10.1093/eurheartj/ehz387.
[52] L. Zhang, L. Xiong, L. Fan, H. Diao, M. Tang, E. Luo, W. Guo, X. Yang, S. Xing, Vascular lipidomics analysis reveales increased levels of phosphocholine and lysophosphocholine in atherosclerotic mice, Nutr. Metab. 20 (2023) 1, https://doi.org/10.1186/s12986-022-00723-y [pii].
[53] D. Zhang, W. Tang, P.M. Yao, C. Yang, B. Xie, S. Jackowski, I. Tabas, Macrophages deficient in CTP:Phosphocholine cytidylyltransferase-alpha are viable under normal culture conditions but are highly susceptible to free cholesterol-induced death, J. Biol. Chem. 275 (2000) 35368–35376, https://doi.org/10.1074/jbc.M007099200. S0021-9258(20)88839-5 [pii].
[54] I. Tabas, S. Marathe, G.A. Keesler, N. Beatini, Y. Shiratori, Evidence that the initial up-regulation of phosphatidylcholine biosynthesis in free cholesterol-loaded macrophages is an adaptive response that prevents cholesterol-induced cellular necrosis, J. Biol. Chem. 271 (1996) 22773–22781, https://doi.org/10.1074/jbc.271.37.22773.
[55] Y. Shiratori Ako, T. Tabas, Free cholesterol loading of macrophages stimulates phosphatidylcholine biosynthesis and up-regulation of CTP: phosphocholine cytidylyltransferase, J. Biol. Chem. 269 (1994) 11337–11348, https://doi.org/10.1016/S0021-9258(19)78130-7.
[56] A. Kadl, A.K. Meher, P.R. Sharma, M.Y. Lee, A.C. Doran, S.R. Johnstone, M. R. Elliott, F. Gruber, J. Han, W. Chen, et al., Identification of a novel macrophage phenotype that develops in response to atherogenic phospholipids via Nrf2, Circ. Res. 107 (2010) 737–746, https://doi.org/10.1161/CIRCRESAHA.109.215715.
[57] P. Libby, P.M. Ridker, A. Maseri, Inflammation and atherosclerosis, Circulation 105 (2002) 1135–1143, https://doi.org/10.1161/hc0902.104353.
[58] S. Lehti, S.D. Nguyen, I. Belevich, H. Vihinen, H.M. Heikkilä, R. Soliymani, R. Käkelä, J. Saksi, M. Jauhiainen, G.A. Grabowski, et al., Extracellular lipids accumulate in human carotid arteries as distinct three-dimensional structures and have proinflammatory properties, Am. J. Pathol. 188 (2018) 525–538, https://doi.org/10.1016/j.ajpath.2017.09.019.
[59] S.L. Schissel, X. Jiang, J. Tweedie-Hardman, T. Jeong, E.H. Camejo, J. Najib, J. H. Rapp, K.J. Williams, I. Tabas, Secretory sphingomyelinase, a product of the acid sphingomyelinase gene, can hydrolyze atherogenic lipoproteins at neutral pH. Implications for atherosclerotic lesion development, J. Biol. Chem. 273 (1998) 2738–2746, https://doi.org/10.1074/jbc.273.5.2738.
[60] S.L. Schissel, J. Tweedie-Hardman, J.H. Rapp, G. Graham, K.J. Williams, I. Tabas, Rabbit aorta and human atherosclerotic lesions hydrolyze the sphingomyelin of retained low-density lipoprotein. Proposed role for arterial-wall sphingomyelinase in subendothelial retention and aggregation of atherogenic lipoproteins, J. Clin. Invest. 98 (1996) 1455–1464, https://doi.org/10.1172/JCI118934.
[61] Holopainen, Sphingomyelinase activity of LDL: a link between atherosclerosis, ceramide, and apoptosis? Trends Cardiovasc. Med. (2002) 37–42.
[62] J.M. Holopainen, O.P. Medina, A.J. Metso, P.K. Kinnunen, Sphingomyelinase activity associated with human plasma low density lipoprotein, J. Biol. Chem. 275 (2000) 16484–16489, https://doi.org/10.1074/jbc.275.22.16484.
[63] T.T.D. Luong, R. Tuffaha, M. Schuchardt, B. Moser, N. Schelski, B. Boehme, C. Gollmann-Tepekoylu, C. Schramm, J. Holfeld, B. Pieske, et al., Acid sphingomyelinase promotes SGK1-dependent vascular calcification, Clin. Sci. 135 (2021) 515–534, https://doi.org/10.1042/CS20201122.
[64] A.N. Kapustin, M.L. Chatrou, I. Drozdov, Y. Zheng, S.M. Davidson, D. Soong, M. Furmanik, P. Sanchis, R.T. De Rosales, D. Alvarez-Hernandez, et al., Vascular smooth muscle cell calcification is mediated by regulated exosome secretion, Circ. Res. 116 (2015) 1312–1323, https://doi.org/10.1161/CIRCRESAHA.116.305012.
[65] O.M. Bhat, X. Yuan, C. Cain, F.N. Salloum, P.L. Li, Medial calcification in the arterial wall of smooth muscle cell-specific Smpd1 transgenic mice: a ceramide-mediated vasculopathy, J. Cell Mol. Med. 24 (2020) 539–553, https://doi.org/10.1111/jcmm.14761.
[66] S.L. Schissel, E.H. Schuchman, K.J. Williams, I. Tabas, Zn2+-stimulated sphingomyelinase is secreted by many cell types and is a product of the acid sphingomyelinase gene, J. Biol. Chem. 271 (1996) 18431–18436, https://doi.org/10.1074/jbc.271.31.18431.
[67] John D. Vickers Rlk-R, J. Fraser Mustard, Phosphatidylinositol 4,5-bisphosphate is selectively retained by platelet-fibrin clots formed by thrombin, J. Biochem. 245 (1987) 649–653.
[68] J.M. Heraud, C. Racaud-Sultan, D. Gironcel, C. Albiges-Rizo, T. Giacomini, S. Roques, V. Martel, M. Breton-Douillon, B. Perret, H. Chap, Lipid products of phosphoinositide 3-kinase and phosphatidylinositol 4',5'-bisphosphate are both required for ADP-dependent platelet spreading, J. Biol. Chem. 273 (1998) 17817–17823, https://doi.org/10.1074/jbc.273.28.17817.
[69] C. Valet, M. Levade, M. Bellio, M. Caux, B. Payrastre, S. Severin, Phosphatidylinositol 3-monophosphate: a novel actor in thrombopoiesis and thrombosis, Res Pract Thromb Haemost 4 (2020) 491–499, https://doi.org/10.1002/rth2.12321.
[70] K. Nagy, V.V. Brahmbhatt, O. Berdeaux, L. Bretillon, F. Destaillats, N. Acar, Comparative study of serine-plasmalogens in human retina and optic nerve: identification of atypical species with odd carbon chains, J. Lipid Res. 53 (2012) 776–783, https://doi.org/10.1194/jlr.D022962.